

PAPER

Silicon eccentric shell nanoparticles fabricated by template-assisted deposition for Mie magnetic resonances enhanced light confinement

To cite this article: Huan Yang *et al* 2024 *Nanotechnology* **35** 235301

View the [article online](#) for updates and enhancements.

You may also like

- [Strong light confinement and optical force enhancement in phosphorene with acoustic plasmons](#)
Hao-yu Wang, Rui Ma, Gui-dong Liu et al.
- [Analytical Model for Sandwich-Lithiation in Hollow Amorphous Silicon Nano-Anodes Coated on Carbon Nanofibers](#)
Xiangdong Li, Qihong Fang, Jia Li et al.
- [Design and analysis of a position chirped metamaterial photonic crystal array for confinement of light pulses](#)
Kisalaya Chakrabarti, Shahriar Mostufa and Alok Kumar Paul



PRIME
PACIFIC RIM MEETING
ON ELECTROCHEMICAL
AND SOLID STATE SCIENCE

HONOLULU, HI
Oct 6–11, 2024

Abstract submission deadline:
April 12, 2024

Learn more and submit!



Joint Meeting of

The Electrochemical Society
•
The Electrochemical Society of Japan
•
Korea Electrochemical Society

Silicon eccentric shell nanoparticles fabricated by template-assisted deposition for Mie magnetic resonances enhanced light confinement

Huan Yang^{1,2,*}, Xinbing Jiang³, Manman Zhang⁴, Ben Q Li⁵, Jiajie Wang¹ and Yiping Han^{1,*}

¹ School of Physics, Xidian University, Xi'an, 710071, People's Republic of China

² Guangzhou Institute of Technology, Xidian University, Guangzhou, 510555, People's Republic of China

³ School of Chemistry, Xi'an Jiaotong University, Xi'an, 710049, People's Republic of China

⁴ Department of Mechanical Engineering, University of Michigan, Dearborn, MI, 48128, United States of America

⁵ State Key Laboratory for Manufacturing Systems Engineering, Xi'an Jiaotong University, Xi'an, 710049, People's Republic of China

E-mail: yanghuan@xidian.edu.cn and yphan@xidian.edu.cn

Received 11 January 2024, revised 21 February 2024

Accepted for publication 28 February 2024

Published 18 March 2024



Abstract

We report a structure of silicon eccentric shell particles array, fabricated by the SiO₂ particles monolayer array assisted deposition of amorphous Si, for high-efficiency light confinement. The SiO₂ particles monolayer array is tailored to regulate its interparticle distance, followed by silicon film deposition to obtain silicon eccentric shell arrays with positive and negative off-center distance e . We studied the Mie resonances of silicon solid sphere, concentric shell, eccentric shell and observed that the eccentric shell with positive off-center e supports superior light confinement because of the enhanced Mie magnetic resonances. Spectroscopic measurements and finite difference time domain simulations were conducted to examine the optical performance of the eccentric shell particles array. Results show that the Mie magnetic resonance wavelength can be easily regulated by the size of the inner void of the silicon shell to realize tunable enhanced light confinement. It was found silicon shell with $D = 460/520$ nm offered high enhanced light absorption efficiency at wavelength of $\lambda = 830$ nm, almost beyond the bandgap of the amorphous silicon.

Supplementary material for this article is available [online](#)

Keywords: pattern and nanostructure, mie magnetic resonances, silicon eccentric shells, light confinement

Introduction

Nanoparticles (NPs) of high refractive index materials offering Mie resonances in the visible to near infrared range have been widely explored to manipulate light-matter interaction at the nanoscale [1, 2]. The high-index NPs naturally sustaining

intense magnetic and electric Mie resonances opens the way to extraordinary properties such as cloaking, negative refraction, sensing, perfect lensing, and broadband total transmission or reflection [3–6]. Among high-index dielectrics, Silicon (Si) is the most attractive material because of its high compatibility to semiconductor industry, as well as the high environmental friendliness, earth abundance, etc. To date, Si NPs have worked as a nanoantenna to enhance the absorption [7–9], emission

* Authors to whom any correspondence should be addressed.

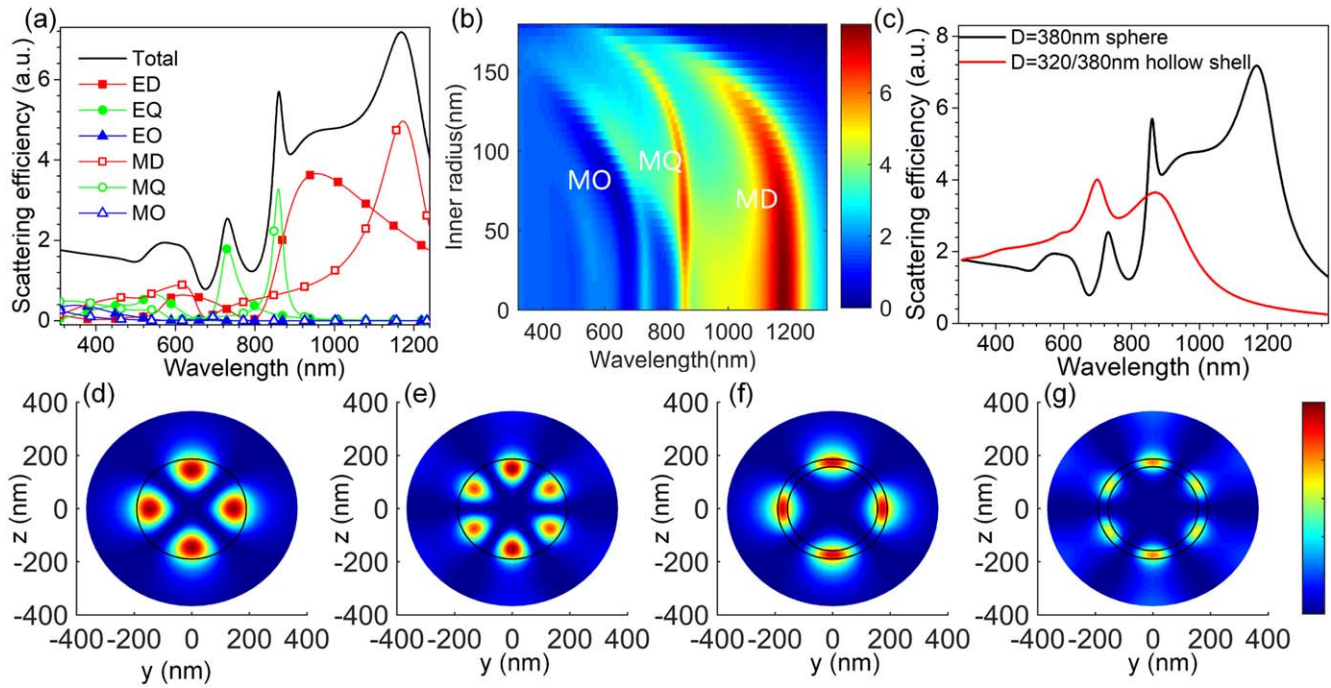


Figure 1. Scattering efficiency and electric field distributions of silicon sphere and shell, (a) total and its contributions of electric modes and magnetic modes of scattering efficiency for $D = 380$ nm silicon sphere, (b) the scattering efficiency of the silicon shell particles as a function of the free-space wavelength and inner void radius, (c) scattering curves of $D = 380$ nm silicon sphere and $D = 320/380$ nm hollow shell, electric field distribution for $D = 380$ nm sphere at wavelength of $\lambda = 1172$ nm (d) and $\lambda = 858$ nm (e) of MD and MQ resonance, the electric field distribution for $D = 320/380$ nm hollow shell at wavelength of $\lambda = 872$ nm (f) and $\lambda = 697$ nm (g) of MD and MQ resonances, respectively.

[10–12], Raman scattering [13–16], and to control the phase and propagation direction of light [1, 17–19].

Spherical silicon particles exhibit well separated electric and magnetic resonances, which results in wavelength dependent angular scattering and light confinement. Merging these resonances is of considerable interest to enable high efficiency broadband light management. It is demonstrated the electric and magnetic Mie resonances can be overlapped by employing clusters of particles, introducing shape anisotropy or designing a core-shell structure [20, 21]. Valagiannopoulos *et al* have theoretically explored the core-shell nanospheres under visible light to achieve optimal absorption and scattering by the size and dielectric constant dependent Mie resonances [22]. As recently reported, Si NPs are usually fabricated by several methods such as laser ablation of bulk Si targets [23–25], mechanical grinding [26], decomposition of silane [27] and chemical vapor deposition [28], etc. All of the core-shell particles are basically fabricated by coating a dielectric or noble metal shell on Si NPs to realize fascinated light management [29, 30]. For instance, Tsuchimoto *et al* demonstrated core-shell Si@SiO₂ particles with a forward-to-backward scattering ratio five times higher than the bare Si particle [31]. Aymonier *et al* prepared NPs colloid of silicon core coated by a lower index silicon oxynitride shell to generate broadband forward scattering by well-regulated Mie resonances [32]. However, to date, no report exists for the synthesis of silicon shell particles and the silicon shell particles array to evaluate their resonant performance.

In this paper, we present a templated assisted deposition method for fabricating the silicon eccentric shell colloid and well-arranged silicon eccentric shell monolayer with enhanced magnetic resonances. The process involves patterning and tailoring a monolayer of the SiO₂ array controllable interparticle distance as a template, followed by Si film deposition to obtain silicon eccentric shell array with positive and negative off-center distance e . We theoretically study the Mie resonances of silicon shell particles, and describe the fabrication process of the silicon eccentric shell particle colloid and well-organized silicon eccentric shell arrays. Then the optical performance of these silicon shells is investigated by means of visible-NIR spectroscopy and FDTD simulations. It is shown that the silicon eccentric shell can be applied to enhance the light confinement of wavelength near or almost beyond the bandgap by size dependent magnetic resonances.

Theoretical analysis

We begin by numerically examining the scattering of a solid silicon sphere with diameter $D = 380$ nm (figure 1(a)), as well as the silicon hollow shells with gradually increasing inner void. Throughout the entire work, the silicon discussed is amorphous silicon and the refractive index was acquired by ellipsometer-measured amorphous silicon film deposited in our laboratory (see figure S1 in supplementary File). The computation of the Mie scattering was executed by solving

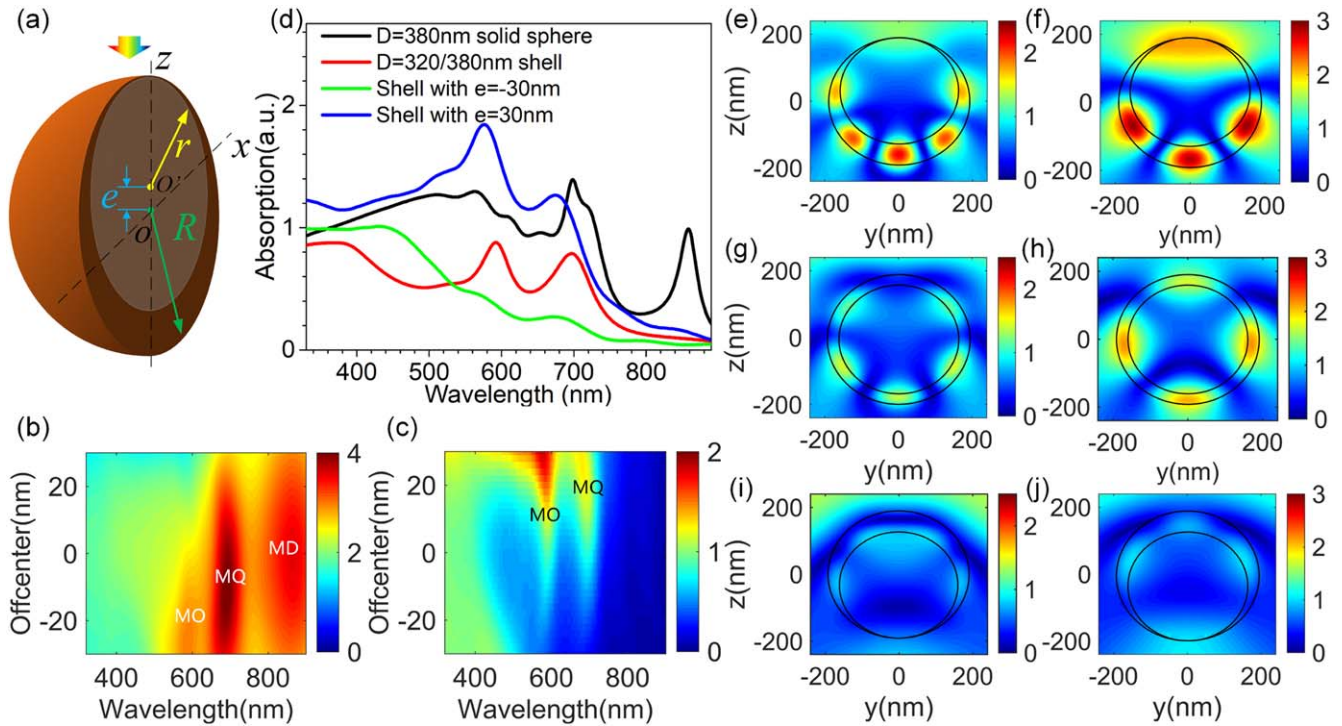


Figure 2. The optical responses of silicon eccentric shell. (a) The schematic of silicon eccentric shell, the scattering (b) and absorption (c) efficiency of $D = 320/380$ nm silicon eccentric shell as a function of off-center distance e , (d) the absorption curves of $D = 380$ nm silicon shell and $D = 320/380$ nm shell and crescent shell with $e = 30$ nm and $e = -30$ nm, the electric field of shell on octupole and quadrupole magnetic resonance with $e = 30$ nm (e), (f), $e = 0$ (g), (h) and $e = -30$ nm (i), (j).

the Maxwell functions of the silicon shell illuminated by plane wave to calculate the total scattering efficiency and multipole decomposition [33]. Figure 1(a) shows that the contributions from each multipole to the total scattering efficiency had a resonance-shape dependence on the wavelengths. These resonances are narrow and well-separated, so one can get magnetic dipole (MD), electric dipole (ED), and high-order multipole scattering, i.e. magnetic quadrupole (MQ) and electric quadrupole (EQ), magnetic octupole (MO) and electric octupole (EO) for a silicon solid sphere. For the silicon shell, as figure 1(b) shows, the total scattering efficiency as well as the contributions from each multipole moment decreases by introducing the void. As a comparison, the silicon shell's the magnetic resonance modes become broader and the electric modes are suppressed. It is due to the inner void dependent merging of the electric and magnetic resonances. It is worth mentioning that the multipole resonance terms are blue-shifted so that the contributions from multipole resonances grow with the size increase of the void in the visible band. The electric field distributions of $D = 380$ nm silicon sphere and the $D = 320/380$ nm silicon shell were calculated at their MD and MQ resonance modes wavelength, respectively. As shown in figures 1(d) and (e), it revealed that the magnetic resonances caused enhanced electric field hot spots were only located in the outer part closing to the surface of the solid sphere. When the silicon solid sphere became a silicon shell with size of $D = 320/380$ nm, the electric field hot spots were compressed within the thin shell of the silicon shell with comparable strength (see figures 1(f) and (g)). As a result, the silicon thin shell

particles are found to more efficiently support broad magnetic resonance modes than silicon solid spheres.

As discussed above, the silicon shells have shown superior performance in efficient light confinement than silicon solid sphere in the visible band. When the inner void of silicon shell moves slightly inside the silicon, a silicon eccentric shell was modeled. As figure 2(a) shows, the silicon eccentric shell was composed of the outer shell with radius R and the inner void with radius r . The off-center distance of these two spheres was noted as e . The silicon eccentric shell particle was illuminated by a plane wave along the z axis, where the off-center e was coincided with the z axis. The scattering and absorption efficiencies of $D = 320/380$ nm silicon shell with varying e were explored.

It was found that the off-center distance e was a key parameter to regulated the scattering and absorption efficiency. As the scattering and absorption efficiency shown in figures 2(b) and (c), the silicon shell got optimal scattering efficiency roughly with the off-center $e = 0$ nm, and then gradually reduced with the change of e . As for the absorption efficiency, the peaks of MQ and octupole resonance modes were clearly defined, while the dipole resonance mode was too weak to distinguish because of the tiny dielectric constant of the silicon at the near infrared band. The MQ and MO resonances reach their maximum when $e = 30$ nm, and then reduced with the decrease of e . It indicated that the eccentric shell could achieve high absorption efficiency when $e = 30$ nm in broadband wavelength from 300 to 700 nm. Besides, the silicon shell with $e = -30$ nm obtained higher scattering efficiency, especially at resonance wavelengths. Therefore, it

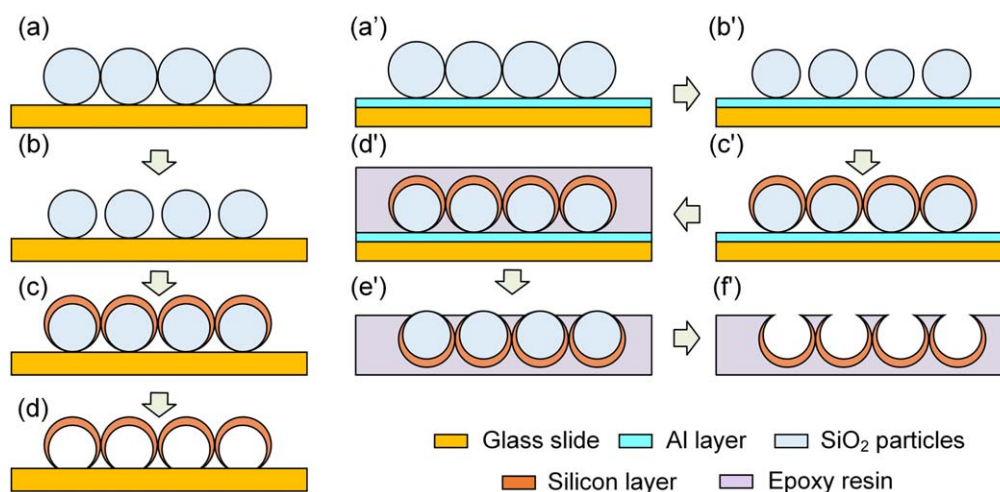


Figure 3. Schematic of silicon eccentric shell arrays' fabrication process.

reveals that the smaller e , i.e. inner hollow cavity moving down along z axis, will depress the absorption and enhance the scattering efficiency.

The absorption efficiency of $D = 380$ nm silicon solid sphere, $D = 320/380$ nm concentric shell and eccentric shell with off-center $e = 30$ nm and -30 nm were examined and presented in figure 2(d). It was found the silicon eccentric shell with $e = 30$ nm shown superior light absorption in the visible band than any other case of the silicon shell, and even better than the solid silicon sphere. The electric field distribution of MQ and MO resonances for the silicon shells with $e = 30$ nm, $e = 0$ and $e = -30$ nm were inspected in figures 2(e)–(j), respectively.

Experimental section

Anhydrous ethanol was purchased from Tianjin Tianli Chemical Company Limited (Tianjin, China). Tetraethyl orthosilicate (TEOS, 98%) was purchased from Sigma-Aldrich. Hydrofluoric acid (HF, 40%) and ammonium hydroxide solution (NH₄OH, 25wt%) were obtained from Aladdin chemistry (Shanghai, China). Hydrochloric acid (HCl, 36%) was purchased from Beijing chemical works (Beijing, China). Ultrapure water (18.25 MΩ·cm) was produced using Millipore water purification system. All reagents were used as received without further purification.

The SiO₂ particles colloid was prepared by the Stöber method [34]. The diameter of the particles was regulated by adjusting the volume ratio of the TEOS, ammonium hydroxide solution, ultrapure water (H₂O) and ethanol. Typically, 8 ml ammonium hydroxide solution was added to 25 ml ethanol and stirring kept for 30 min to make them uniformly mixed. 2 ml TEOS was then quickly added to the mixture. The solution was stirred for 8 h to obtain SiO₂ colloids with diameter of ~ 390 nm. By increasing the TEOS to 3 ml, $D = \sim 460$ nm SiO₂ particles colloid was obtained. Furthermore, when the 8 ml ammonium hydroxide solution was substituted by a mixture of 3 ml ammonium hydroxide solution and 3 ml H₂O in this reaction, the well dispersed SiO₂

particles of $D = 520$ nm was prepared. A monolayer of closely arranged SiO₂ particles array was obtained at water/air interface and transferred to a substrate, with the detailed procedures introduced in our previous work [35].

The silicon eccentric shell particles monolayer array was fabricated via the templated-assisted deposition method. The fabrication process was briefly illustrated in figure 3. A closely arranged SiO₂ particles monolayer was firstly prepared on the substrate (see figure 3(a)). The substrate was a pre-cleaned glass slide, which was treated by oxygen plasma to make the surface hydrophilic. It should be noted that the interparticle space of the SiO₂ particles monolayer is too small to obtain independently silicon shell particles by directly depositing the silicon film. Therefore, the size of SiO₂ particles was reduced to tune the interparticle space of the SiO₂ particles monolayer (figure 3(b)).

After that, the SiO₂/Si core/shell particles monolayer array was fabricated by coating a ~ 60 nm silicon film. The amorphous silicon film deposition was executed in the Orion III plasma-enhanced CVD system from Trion Technology, Inc. (see figure S2 in supplement file). The deposition chamber with samples loaded was heated and vacuumed to reach the low pressure of ~ 2 mTorr and the high temperature of 350°C . Then the gases of Ar and SiH₄ were introduced into the chamber with the flow rate of 250 and 10 standard cubic centimeters (SCCM), respectively. The RF (radio frequency) power was set as 75 W to start the silicon deposition process, making sure the RF reflected power lower than 15 W. During the process, the chamber pressure was kept as 600 mTorr. The deposition process last for 600 s to obtain the silicon eccentric shell with maximum thickness of 60 nm.

Since the reactive species are accelerated perpendicularly to the sample in a unidirectional electric field in the deposition chamber, the density of the accessible ionized gases decreased from the upper surface to the lower surface of the SiO₂/a-Si particles. Therefore, the thickness of the coated Si film gradually decreases to zero along the direction from the top of the particle to the contact point between the particle and the substrate (see figure 3(c)). The SiO₂ cores were then removed by immersing the sample in diluted hydrofluoric

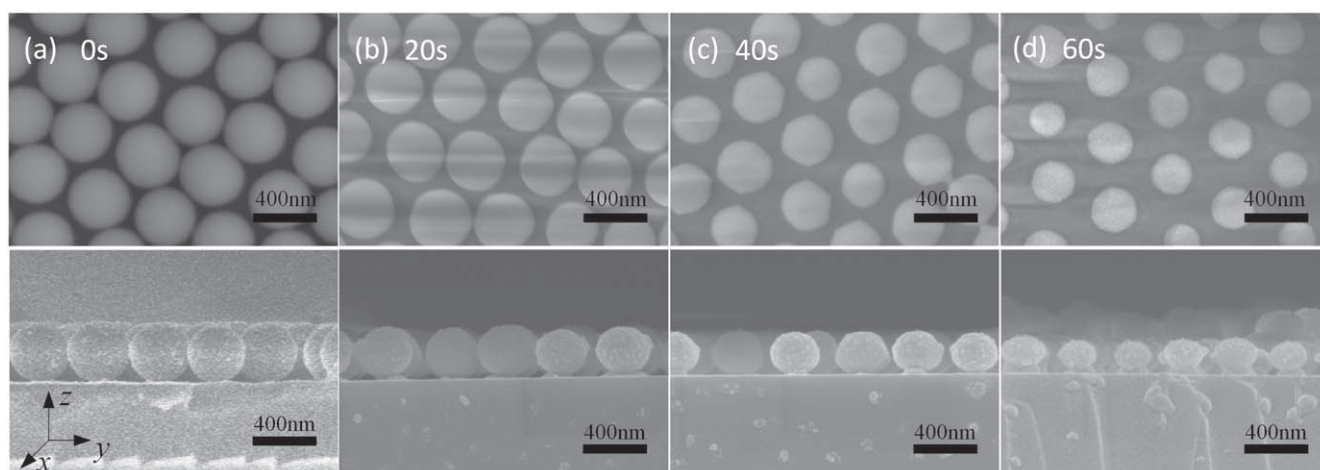


Figure 4. SEM of SiO₂ monolayer array with varying etching time.

acid (5% v/v) for 7 s. Finally, as shown in figure 3(d), an up-right eccentric silicon hollow shell array was obtained by drying the samples in an oven of 60 °C.

A glass substrate was firstly coated with 200 nm Al film as sacrifice layer (see figure 3(a')). The Al film coating processes are carried out in a vacuum chamber at a base pressure of 0.8×10^{-6} mbar and room temperature with the magnetron sputtering system (Denton Vacuum Explorer 14). The chamber was then filled with pure argon gas with a flow rate of 20 SCCM and the deposition of Aluminum film was performed at 1000 W by using DC power supply. In order to obtain uniform Al film, the samples were fixed on the rotary table of the chamber with a rotation rate of 4rpm. The deposition process lasts for 300 s to obtain 200 nm thick Al film. The SiO₂/Si core-shell particles array on Al film was obtained after the procedure of SiO₂ size reduction and ~60 nm silicon film deposition (see figures 3(b'), (c')). An epoxy resin layer (~2 mm) then was coated on the samples by letting a resin droplet undergo free spreading, followed by curing at 55 °C for an hour (see figure 3(d')). Then the SiO₂@Si core-shell monolayer array was transferred to epoxy resin layer by releasing the Al film in diluted hydrochloric acid (10% v/v). Inverting the epoxy layer exposes to air, an array of up-right Si shells coated on the SiO₂ particles (see figure 3(e')). The SiO₂ cores were then removed by immersing the sample in diluted hydrofluoric acid (5% v/v) for 150 s, leaving as the final product of an array of inverted Si eccentric shell array (figure 3(f')).

The interparticle space of the SiO₂ monolayer array was tailored by reducing the size of the individual SiO₂ particle with reactive ion etcher (Oxford Plasmalab 180). Specifically, the sample of SiO₂ particles monolayer array was loaded into a chamber at a pressure of 10 mTorr. Gases of SF₆ and Ar were charged into the chamber with flow rates of 60 and 30 SCCM, respectively, to generate reactive ions. RF power and ICP power of 50 W and 500 W were applied, respectively. After that, the interparticle distance of SiO₂ particles in the monolayer depended on the etching time durations.

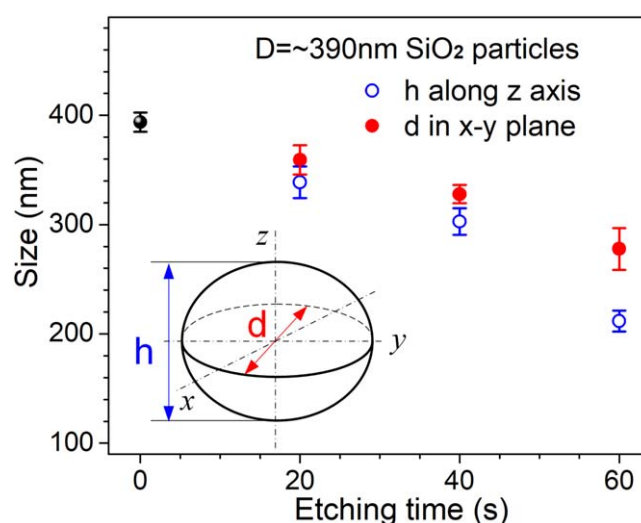


Figure 5. Size analysis of etched SiO₂ nanoparticles.

Results and discussions

Figure 4 shows both the normal (upper row) and cross-sectional view (lower row) of the $D = 390$ nm SiO₂ particles monolayer array with the etching times of $t = 0, 20$ s, 40 s, and 60 s, respectively. The SEM image at $t = 0$ s shows the morphology of the pristine sample of the SiO₂ spherical particle monolayer arrays (see figure 4(a)). With the etching time t increases, SiO₂ particles' size decreased at anisotropic etching rate along x - y plane and z axis. As shown in figure 4(d), The SiO₂ particles were gradually developed into ellipsoid from sphere in appearance with faster etching rate along z axis, which was explained by the anisotropic density of the accessible ionized gases in the etching process [36].

The size of SiO₂ particles at various etching stages was recorded and statistically analyzed. As figure 5 show, the etched SiO₂ particles' height h along z axis and diameter d at x - y plane were measured. It indicated that the SiO₂ particles' size decreased at nearly constant etching rates of 2 nm s^{-1} along z direction, 1.25 nm s^{-1} at the x - y direction within 40 seconds, respectively. When the etching process goes

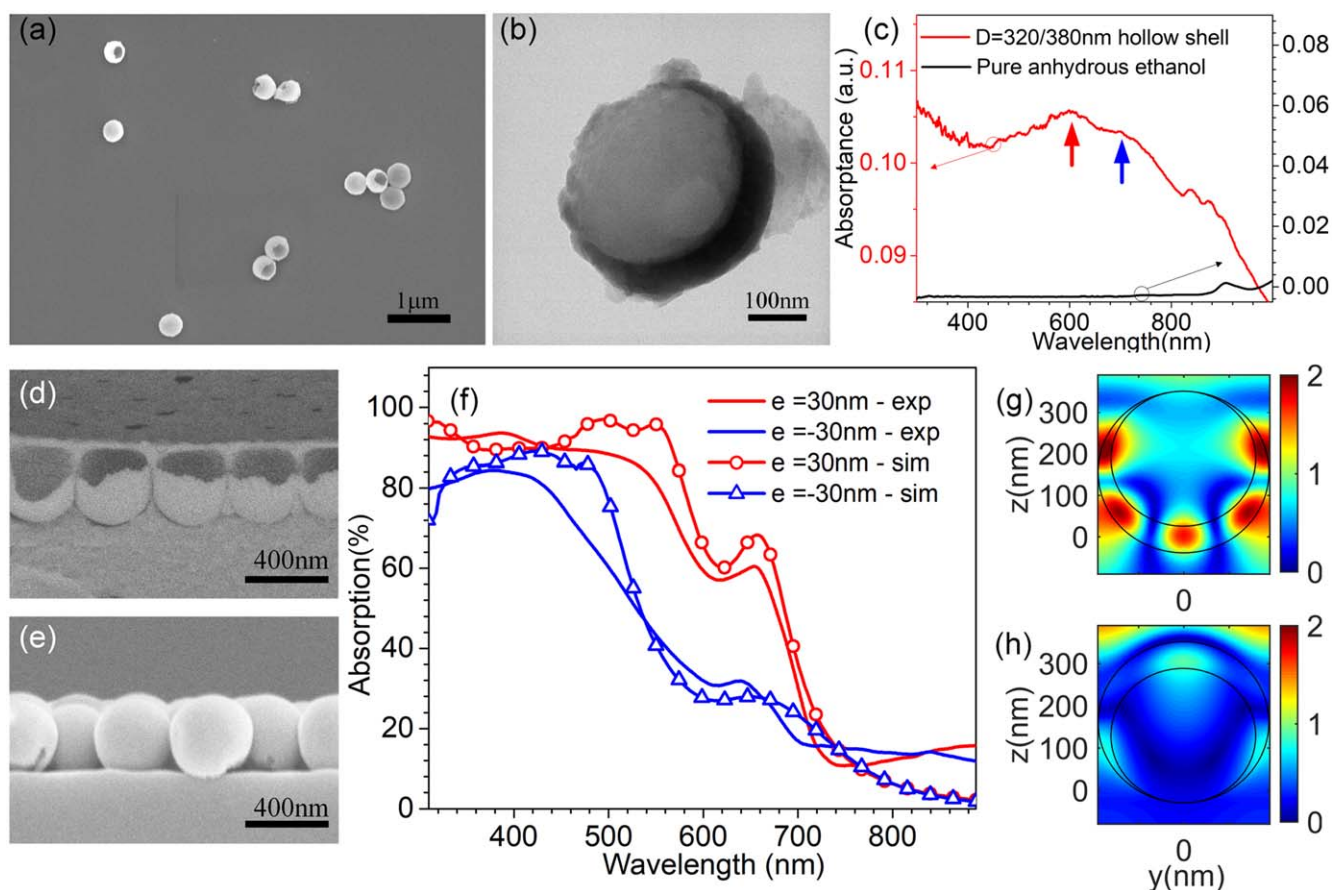


Figure 6. Characterization and optical response of silicon eccentric shells, SEM (a), TEM (b) images, measured absorbance curves of $D = 320 \text{ nm}/380 \text{ nm}$ silicon shell colloidal and ethanol (c), morphology of silicon shell monolayer array with $e = 30 \text{ nm}$ (d) and $e = -30 \text{ nm}$ (e), the absorption curves (f) of the silicon shell monolayer arrays, and the electric field distribution of silicon shell with $e = 30 \text{ nm}$ (g) and $e = -30 \text{ nm}$ (h) at their magnetic quadrupole resonance wavelengths, respectively.

beyond 40 s, the spherical SiO_2 particles were tailored to be oblate ellipsoid in appearance, by distinctively enhanced etching rate of 4.5 nm s^{-1} at z direction. In this work, the structure of silicon eccentric shell with spherical inner cavity was discussed. Therefore, the size of SiO_2 particles in the monolayer were slightly reduced by etching 40 s to make sure that a well-separated silicon shell particles array was fabricated by the silicon shell coating process.

Based on the silicon eccentric hollow shell array shown in figure 3(d), the silicon shell particles colloid was acquired by immersing the silicon eccentric hollow shell array in anhydrous ethanol with sonication. As shown in figure 6(a), the morphology of the silicon shell particles was characterized by SEM. It was found that the eccentric silicon shell particles were well dispersed and uniform in size. There was an open pole in almost each of the eccentric shells, which was ascribed to the damage by the strong sonication process to lift off the silicon shells from the substrate. A broken silicon shell was found and inspected by TEM, which happened to clearly present the structure of the silicon eccentric shell. As figure 6(b) shows, there was a decrease in shell thickness from one pole to the other.

The optical response of the silicon shell colloid was detected by the UV-vis spectrophotometer (Shimadzu UV-

3600), with ethanol as the baseline (see figure 6(c)). The absorbance of ethanol was also examined. It was found there were several peaks in the absorbance curve of the silicon shell, which were related to the resonance modes of the silicon eccentric shell particles. As a comparison to with the simulated results shown in figure 2(d), the MQ and octupole resonance peaks were marked by the blue and red arrow, respectively. It was found that the measured and theoretical MD and MQ resonances were almost consistent in peak wavelengths. However, the resonance peaks in the measured curve was not so distinct as the numerical results.

As presented in figure 2(d), the eccentric shell with the off-center $e = 30 \text{ nm}$ achieved an optimal absorption efficiency when the shell particle was illuminated as shown in figure 2(a). In fact, the silicon eccentric shell particles dispersed in the ethanol were randomly oriented. Consequently, the measured absorption curve was an averaged evaluation to the orientation dependent performance of all the silicon eccentric shell particles. Therefore, the measure magnetic resonance peaks were much flatter than that in the simulated curve. It should be noted that the MO resonance was much stronger than the MQ resonance in the measured curve, which agree well with the numerical results presented in figure 2(d). Besides, there were several extra minor peaks near the

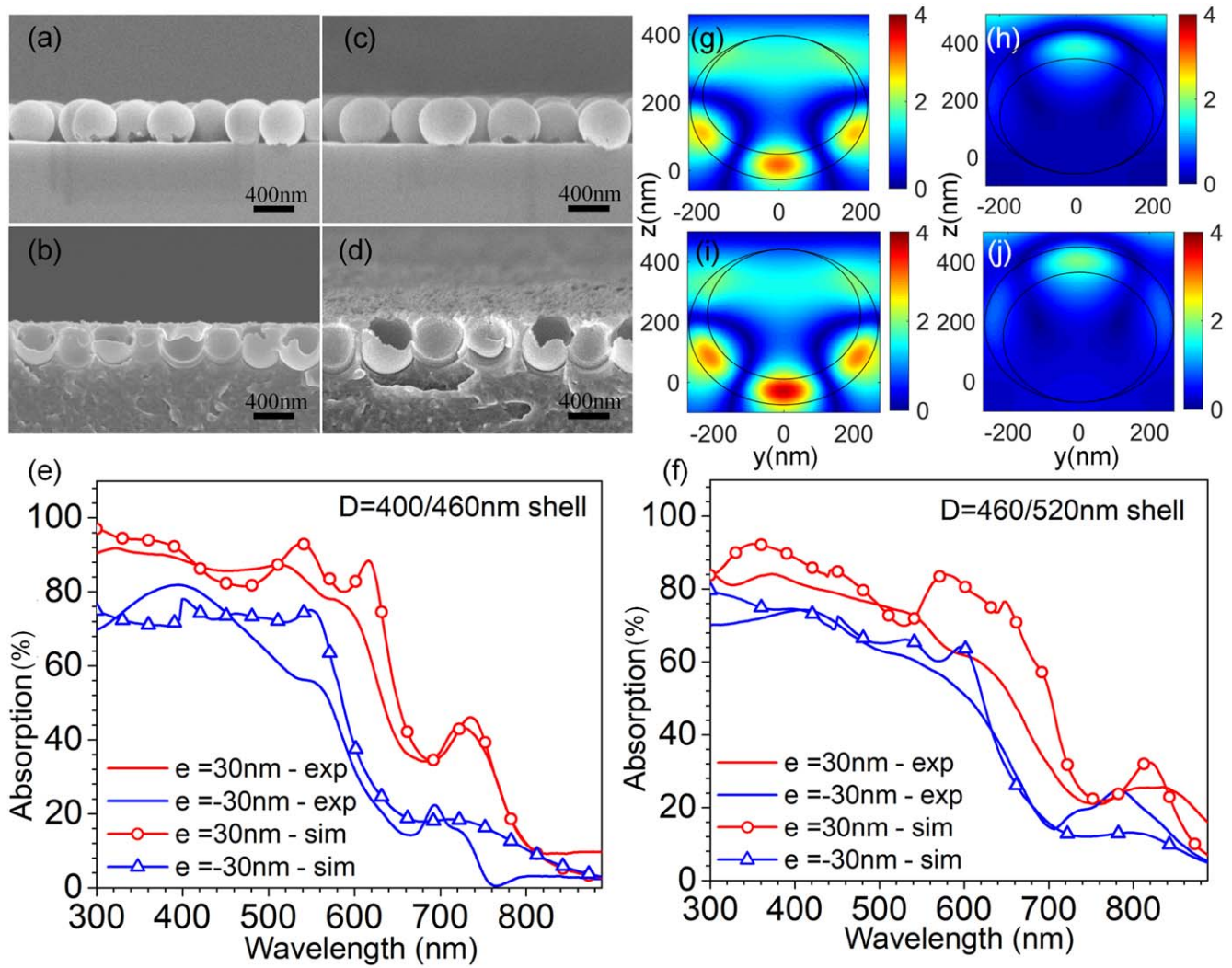


Figure 7. The morphology of $D = 400/460$ nm (a, b) and $D = 460/520$ nm (c, d) eccentric silicon shells, the experimental and simulated absorption curves of $D = 400/460$ nm (e) and $D = 460/520$ nm (f) silicon shell array, the electric field distribution of MO resonance for silicon eccentric shell of $D = 400/460$ nm shell with $e = 30$ nm (g), $e = -30$ nm (h) and $D = 460/520$ nm with $e = 30$ nm (i), $e = -30$ nm (j).

wavelength of $\lambda = \sim 850$ nm in the measured curve, which might be due to coupled resonances of eccentric shell particles aggregation.

Unlike the silicon shell colloid, the silicon eccentric shell array presented well-ordered pattern. As shown in figures 6(d) and (e), the silicon shell arrays with off-center distance of $e = 30$ nm and $e = -30$ nm were prepared by the method introduced in figure 3. The FDTD simulations of $D = 320/380$ nm silicon eccentric shell array were carried out using the commercial software of Lumerical to evaluate its optical response. In the model, periodic boundary conditions were applied in the x and y directions to simplify the model for the hexagonal arranged shell array. The x -polarized plane wave was incident normally on the structure along the negative direction of z . The absorption efficiency of the $D = 320$ nm/ 380 nm silicon shell with $e = 30$ nm (red) and $e = -30$ nm (blue) was theoretically and numerically inspected in the wavelength band of 300–900 nm.

The uniformly patterned silicon eccentric shell array showed strong capacity of light confinement with distinct resonance peaks. As figure 6(f) shows, all the experimental results were generally in good consistent with the simulated curves. For the case of silicon shell array with $e = 30$ nm, there was a distinct peak at $\lambda = 650$ nm on the experimental and simulated curves. Then the electric field distribution of the silicon eccentric shell at $\lambda = 650$ nm was examined and shown in figure 6(g). There were five strong electric field spots evenly located inside the silicon shell except for the north pole of the silicon shell. The shell thickness near the north pole was too thin to trap the incident light. Therefore, the enhanced absorption was ascribed to the enhanced MO resonance of the silicon eccentric shell with $e = 30$ nm. Since the eccentric shell with increasing shell thickness along the incident direction, the silicon shell array worked as antireflection film to realize outstanding light absorption in the wavelength band of 300–600 nm.

While for the case of the silicon shell array with $e = -30$ nm, the absorption efficiency was much lower in the entire wavelength band (figure 6(f)). There was a flat peak also occurred at the wavelength of $\lambda = 648$ nm caused by the MO resonance. As shown in figure 6(h), the electric field was much lower within the silicon eccentric shell with $e = -30$ nm, resulting in poor light confinement. It was indicated that the eccentric silicon shell with $e = 30$ nm supported high-efficient light confinement in the entire wavelength band and much better than the case of $e = -30$ nm.

As discussed above, the resonance wavelength of the magnetic mode depends on the size of the silicon shell. The eccentric shell with larger inner void size were also fabricated to examine their magnetic resonance enhanced light confinement. The SiO₂ particles of $D = 460$ nm and $D = 520$ nm were applied with the fabrication process shown in figure 3. Then the silicon eccentric shell array with $D = 400/460$ nm and $D = 460/520$ nm were fabricated and examined by SEM (see figures 7(a)–(d)). The cross section of the silicon eccentric shell showed the well patterned structure. The absorption of these silicon shell was examined and presented in figures 7(e) and (f), which indicated the absorption peak wavelength and the enhanced absorption efficiency redshifted from 740 to 830 nm with the size increasing from $D = 400/460$ nm and $D = 460/520$ nm. The electric field distribution at their resonance peak wavelengths were also examined. As shown in figures 7(g)–(j), it was observed that the strong MO resonance occurred in the silicon eccentric shell particles with $e = 30$ nm. Besides, the intensity of electric field for the silicon eccentric shell increased with the increase of shell's size, when comparing the electric field intensity in figures 6(g), and 7(g)–(i). It is worth mentioning that the silicon extinction coefficient is very small near $\lambda \sim 830$ nm, where is beyond the reported bandgap of a-Si in the range of 1.5–2 eV, i.e. 620–826 nm [37]. Thanks to the MO resonances, the $D = 460/520$ nm silicon eccentric shell with $e = 30$ nm achieved enormously enhanced light absorption efficiency of $\sim 23\%$ at $\lambda = 830$ nm. Therefore, it is concluded that the structure of eccentric shell was a simple and effective dielectric resonator by fine tuning the size and refractive index.

Conclusion and outlooks

In conclusion, we have introduced a SiO₂ nanoparticle monolayer array template assisted silicon deposition method for nanofabricating silicon eccentric nanoshells. The SiO₂ nanoparticles monolayer array was a slightly tailored to worked as templates to prepare well organized arrays. We have studied the Mie resonances of a-Si solid sphere, concentric shell, eccentric shell and observed that the eccentric shell with positive off-center e supports superior light confinement because of the enhanced Mie magnetic resonances. The magnetic resonances can be easily regulated by the size of the inner void of the a-Si shell. It turns out that the magnetic octuple resonance of $D = 460/520$ nm silicon shell offer high enhanced light absorption efficiency at wavelength of $\lambda = 830$ nm, beyond the bandgap of amorphous silicon.

Therefore, the structure of eccentric shell with size dependent magnetic resonances may be useful in resonator, photo-detectors, photocatalysts, or constructing high-efficiency solar cells for light harvesting.

Acknowledgments

The authors acknowledge financial support from the Natural Science Basic Research Program of Shaanxi (Program No. 2023-JC-QN-0586), Guangdong Basic and Applied Basic Research Foundation (2022A15110894) and the Fundamental Research Funds for the Central Universities (XJS222702).

Data availability statement

All data that support the findings of this study are included within the article (and any supplementary files).

ORCID iDs

Huan Yang  <https://orcid.org/0000-0002-7145-8495>
Xinbing Jiang  <https://orcid.org/0000-0002-2490-1992>

References

- [1] Sugimoto H and Fujii M 2021 Colloidal Mie resonant silicon nanoparticles *Nanotechnology* **32** 452001
- [2] Xu J, Wu Y, Zhang P, Wu Y, Vallée R A L, Wu S and Liu X 2021 Resonant scattering manipulation of dielectric nanoparticles *Adv. Opt. Mater.* **9** 2100112
- [3] Molet P, Gil-Herrera L K, Garcia-Pomar J L, Caselli N, Blanco Á, López C and Mihi A 2020 Large area metasurfaces made with spherical silicon resonators *Nanophotonics* **9** 943–51
- [4] Liu W, Li Z, Cheng H and Chen S 2020 Dielectric resonance-based optical metasurfaces: from fundamentals to applications *iScience* **23** 101868
- [5] Bi K, Wang Q, Xu J, Chen L, Lan C and Lei M 2020 All-dielectric metamaterial fabrication techniques *Adv. Opt. Mater.* **9** 2001474
- [6] Shima D, Sugimoto H, Assadillayev A, Raza S and Fujii M 2023 Gallium phosphide nanoparticles for low-loss nanoantennas in visible range *Adv. Opt. Mater.* **11** 2203107
- [7] Odebo Lank N, Verre R, Johansson P and Kall M 2017 Large-scale silicon nanophotonic metasurfaces with polarization independent near-perfect absorption *Nano Lett.* **17** 3054–60
- [8] Priolo F, Gregorkiewicz T, Galli M and Krauss T F 2014 Silicon nanostructures for photonics and photovoltaics *Nat. Nanotechnol.* **9** 19–32
- [9] Yang C Y, Yang J H, Yang Z Y, Zhou Z X, Sun M G, Babicheva V E and Chen K P 2018 Nonradiating silicon nanoantenna metasurfaces as narrowband absorbers *ACS Photon.* **5** 2596–601
- [10] Assadillayev A, Hinamoto T, Fujii M, Sugimoto H, Brongersma M L and Raza S 2021 Plasmon launching and scattering by silicon nanoparticles *ACS Photon.* **8** 1582–91
- [11] Garcia-Guirado J, Svedendahl M, Puigdollers J and Quidant R 2020 Enhanced chiral sensing with dielectric nanoresonators *Nano Lett.* **20** 585–91

- [12] Zhang C Y, Xu Y, Liu J, Li J T, Xiang J, Li H, Li J X, Dai Q F, Lan S and Miroshnichenko A E 2018 Lighting up silicon nanoparticles with Mie resonances *Nat. Commun.* **9** 2964
- [13] Frizyuk K, Hasan M, Krasnok A, Alú A and Petrov M 2018 Enhancement of Raman scattering in dielectric nanostructures with electric and magnetic Mie resonances *Phys. Rev. B* **97** 085414
- [14] Zograf G P, Ryabov D, Rutckaia V, Voroshilov P, Tonkaev P, Permyakov D V, Kivshar Y and Makarov S V 2020 Stimulated Raman scattering from Mie-Resonant subwavelength nanoparticles *Nano Lett.* **20** 5786–91
- [15] Raza S and Kristensen A 2020 Raman scattering in high-refractive-index nanostructures *Nanophotonics* **10** 1197–209
- [16] Yang H, Li B Q, Jiang X B and Shao J Y 2019 Hybrid nanostructure of SiO₂@Si with Au-nanoparticles for surface enhanced Raman spectroscopy *Nanoscale* **11** 13484–93
- [17] Negoro H, Sugimoto H, Hinamoto T and Fujii M 2022 Template-assisted self-assembly of colloidal silicon nanoparticles for all-dielectric nanoantenna *Adv. Opt. Mater.* **10** 2102750
- [18] De Marco M L, Semlali S, Korgel B A, Barois P, Drisko G L and Aymonier C 2018 Silicon-based dielectric metamaterials: focus on the current synthetic challenges *Angew. Chem. Int. Ed. Engl.* **57** 4478–98
- [19] Fu Y H, Kuznetsov A I, Miroshnichenko A E, Yu Y F and Luk'yanchuk B 2013 Directional visible light scattering by silicon nanoparticles *Nat. Commun.* **4** 1527
- [20] Zenin V A *et al* 2020 Engineering nanoparticles with pure high-order multipole scattering *ACS Photon.* **7** 1067–75
- [21] Wang M, Krasnok A, Lepeshov S, Hu G, Jiang T, Fang J, Korgel B A, Alu A and Zheng Y 2020 Suppressing material loss in the visible and near-infrared range for functional nanophotonics using bandgap engineering *Nat. Commun.* **11** 5055
- [22] Sheverdin A and Valagiannopoulos C 2019 Core-shell nanospheres under visible light: Optimal absorption, scattering, and cloaking *Phys. Rev. B* **99** 075305
- [23] Zywiets U, Evlyukhin A B, Reinhardt C and Chichkov B N 2014 Laser printing of silicon nanoparticles with resonant optical electric and magnetic responses *Nat. Commun.* **5** 3402
- [24] Zhang D S, Goekce B and Barcikowski S 2017 Laser synthesis and processing of colloids: fundamentals and applications *Chem. Rev.* **117** 3990–4103
- [25] Sugimoto H and Fujii M 2017 Colloidal dispersion of subquarter micrometer silicon spheres for low-loss antenna in visible regime *Adv. Opt. Mater.* **5** 1700332
- [26] Chaâbani W, Proust J, Movsesyan A, Béal J, Baudrion A L, Adam P M, Chehaidar A and Plain J 2019 Large-scale and low-cost fabrication of silicon mie resonators *ACS Nano* **13** 4199–208
- [27] Shi L, Harris J T, Fenollosa R, Rodriguez I, Lu X T, Korgel B A and Meseguer F 2013 Monodisperse silicon nanocavities and photonic crystals with magnetic response in the optical region *Nat. Commun.* **4** 1904
- [28] Yavas O, Svedendahl M and Quidant R 2019 Unravelling the role of electric and magnetic dipoles in biosensing with Si nanoresonators *ACS Nano* **13** 4582–8
- [29] Zograf G P *et al* 2020 All-optical nanoscale heating and thermometry with resonant dielectric nanoparticles for controllable drug release in living cells *Laser Photon. Rev.* **14** 1900082
- [30] Sugimoto H, Hinamoto T, Kazuoka Y, Assadillayev A, Raza S and Fujii M 2022 Mode hybridization in silicon core-gold shell nanosphere *Small* **18** 2204890
- [31] Tsuchimoto Y, Yano T A, Hada M, Nakamura K G, Hayashi T and Hara M 2015 Controlling the visible electromagnetic resonances of Si/SiO dielectric core-shell nanoparticles by thermal oxidation *Small* **11** 4844–9
- [32] De Marco M L, Jiang T, Fang J, Lacomme S, Zheng Y, Baron A, Korgel B A, Barois P, Drisko G L and Aymonier C 2021 Broadband forward light scattering by architectural design of core-shell silicon particles *Adv. Funct. Mater.* **31** 2100915
- [33] Bohren C F and Huffman D R 1998 *Absorption and Scattering of Light by Small Particles* (Wiley) (<https://doi.org/10.1002/9783527618156>)
- [34] Wang X D, Shen Z X, Sang T, Cheng X B, Li M F, Chen L Y and Wang Z S 2010 Preparation of spherical silica particles by stober process with high concentration of tetra-ethyl-orthosilicate *J. Colloid Interf. Sci.* **341** 23–9
- [35] Yang H, Li B Q, Jiang X B, Yu W and Liu H Z 2017 Nano-fabrication of depth-varying amorphous silicon crescent shell array for light trapping *Nanotechnology* **28** 505301
- [36] Lotito V and Zambelli T 2022 Playing with sizes and shapes of colloidal particles via dry etching methods *Adv. Colloid Interf. Sci.* **299** 102538
- [37] Gaspari F and Quaranta S 2018 Energy Materials *Comprehensive Energy Systems* (Elsevier) (<https://doi.org/10.1016/B978-0-12-809597-3.00215-7>)